Tuning localized plasmons in nanostructured substrates for surface-enhanced Raman scattering

Nicolas M. B. Perney, Jeremy J. Baumberg

School of Physics and Astronomy,
University of Southampton, SO17 1BJ, Southampton, UK
nmbp@phys.soton.ac.uk

Majd E. Zoorob, +Martin D. B. Charlton, *Sven Mahnkopf, Caterina M. Netti

Mesophotonics Ltd.,
2 Venture Road, Chilworth Science Park, SO16 7NP, Southampton, UK
+ School of Electronics and computer Science,
University of Southampton, SO17 1BJ, Southampton, UK
*Now at OptiComp Corporation, 215 Elks Point Road, Zephyr Cove, NV 89448, U.S.A.

Abstract: Comprehensive reflectivity mapping of the angular dispersion of nanostructured arrays comprising of inverted pyramidal pits is demonstrated. By comparing equivalently structured dielectric and metallic arrays, diffraction and plasmonic features are readily distinguished. While the diffraction features match expected theory, localised plasmons are also observed with severely flattened energy dispersions. Using pit arrays with identical pitch, but graded pit dimensions, energy scaling of the localised plasmon is observed. These localised plasmons are found to match a simple model which confines surface plasmons onto the pit sidewalls thus allowing an intuitive picture of the plasmons to be developed. This model agrees well with a 2D finite-difference time-domain simulation which shows the same dependence on pit dimensions. We believe these tuneable plasmons are responsible for the surface-enhancement of the Raman scattering (SERS) of an attached layer of benzenethiol molecules. Such SERS substrates have a wide range of applications both in security, chemical identification, environmental monitoring and healthcare.

References and Links

1. J. J. Baumberg, N. M. B. Perney, M. C. Netti, M. D. B. Charlton, M. Zoorob, and G. J. Parker, "Visible-wavelength Super-refraction in Photonic Crystal Superprisms," Appl. Phys. Lett. **85**, 354-356 (2004).
2. H. Gersen, T. J. Karle, R. J. P. Engelen, W. Bogaerts, J. P. Korterik, N. F. van Hulst, T. F. Krauss, and L. Kuipers, "Real-Space Observation of Ultraslow Light in Photonic Crystal Waveguides," Phys. Rev. Lett. **94**, 073903 (2005)
3. Y. Akahane, T. Asano, B. Song, and S. Noda, " Fine-tuned high-Q photonic-crystal nanocavity," Opt. Express **13**, 1202-1214 (2005), http://www.opticsexpress.org/abstract.cfm?URI=OPEX-13-4-1202
4. William L. Barnes, Alain Dereux and Thomas W. Ebbesen, "Surface plasmon subwavelength optics," Nature **424**, 824-830 (2003)
5. T.A. Kelf, Y. Sugawara, J.J. Baumberg, M. Abdelsalam and P.N. Bartlett, "Plasmonic bandgaps and Trapped Plasmons on Nanostructured Metal Surfaces," Phys. Rev. Lett. **95**, 116802 (2005)

6. Mamdouh E. Abdelsalam, Philip N. Bartlett, Jeremy J. Baumberg, Tim A. Kelf, Suzanne Cintra and Andrea E. Russell, "Electrochemical SERS at a structured gold surface," ElectroChemistry Comm. **7**, 740 (2005)

7. W. L. Barnes, T. W. Preist, S. C. Kitson, and J. R. Sambles, "Physical origin of photonic energy gaps in the propagation of surface plasmons on gratings," Phys. Rev. B, **54**, 6227-6244 (1996).

8. S. Coyle, M.C. Netti, J.J. Baumberg, M.A Ghanem, P.R. Birkin, P.N. Bartlett, D.M. Whittaker, "Confined Plasmons in Metallic Nanocavities," Phys. Rev. Lett. **87**, 176801 (2001)

9. K. Sato, M. Shikida, T. Yamashiro, M. Tsunekawa, and S. Ito, "Roughening of single-crystal silicon: surface etched by KOH water solution," Sens. Actuators A **73**, 122-30 (1999)

10. W.-C. Tan, T.W.P., J. R. Sambles, and N. P. Wanstall, "Flat surface-plasmon-polariton bands and resonant optical absorption on short-pitch metal gratings," Phys. Rev. B, **59**, 12661-12666, (1999)

11. T.V. Teperik, V.V. Popov, F.J.Garcia de Abajo, J.J. Baumberg, T. A. Kelf and Y.Sugawara "Enhancement of surface plasmon-polariton resonances on nanoporous metal surface," submitted to Phys. Rev. Lett. (2005)

12. JJ Baumberg, T. A. Kelf, Y Sugawara, S Pelfrey, M Adelsalam, PN Bartlett, AE Russell, "Angle-Resolved Surface-Enhanced Raman Scattering on Metal Nanostructured Plasmonic Crystals," NanoLett, **11**, 2262-2267 (2005).

13. C. A. Szafranski, W. Tanner, P. E. Laibinis, and R. L. Garrell, "Surface-enhanced Raman spectroscopy of aromatic thiols and disulfides on gold electrodes," Langmuir. **14**, 3570-3579 (1998).

14. C. L. Haynes, R. P. Van Duyne, "Plasmon-Sampled Surface-Enhanced Raman Excitation Spectroscopy," J. Phys. Chem. B, **107**, 7426-7433 (2003).

15. Z.Q. Tian, B. Ren, D.Y. Wu, "Surface-enhanced raman scattering: from noble to transition metals and from rough surfaces to ordered nanostructures," J. Phys. Chem. B., **106**, 9463-9483 (2002).

1. Introduction

The burgeoning interest in nanostructuring of dielectrics to make optical devices with novel properties has resulted in photonic crystals with extreme properties such as super-refraction [1], slow pulse propagation [2], negative refraction, and ultrasmall optical cavities [3]. Similarly, the field of plasmonics is rapidly promising new ways to control the interaction of electromagnetic waves with matter at the nanometre scale. So far the application of choice for plasmonics has been sensing and in particular Surface Plasmon Resonance (SPR) and Surface Enhanced Raman Scattering (SERS). Understanding how Surface Plasmon Polaritons (SPPs) propagate on nanostructured metal surfaces is crucial in developing efficient SPR and SERS substrates. However, although specific localised plasmons are well understood for isolated particles of different shape, and for various grating structures, a general understanding of how plasmons localize on deformed metal surfaces is lacking. This is partly due to the current difficulty of solving Maxwell's equations within the full three dimensional geometries including metallic media. This also is evident in the controversial discussions about the role of plasmons in how light squeezes through sub-wavelength scale holes in metal films [3]. Particularly lacking is a systematic exploration of the localized plasmons in different geometries, resulting in very little intuitive guidance about appropriate nanostructure design [5].

We demonstrate here a new class of plasmonic nanostructures that support trapped plasmons which interact strongly with incident light. Instead of depending on nanoparticles and sharp metallic features, these nanostructures are based on a void architecture. Using comprehensive spectral reflectance measurements on both gold-coated and uncoated nanostructures as a function of incident angle, we measure the dispersion of the different diffraction and plasmon modes which appear. We demonstrate the tuning of the localized plasmon resonances in a range of nanostructures with fixed periodicity but different depths. We are thus able to explain the different origin of localised and delocalised plasmon modes, and provide a simple intuitive model that accounts for their energies based on plasmon standing waves in concave geometries. We show that by careful engineering of the metallic surface it is possible to tune the plasmon bands to be resonant with the excitation wavelength found in common Raman spectrometers (e.g., 633nm, 785nm). We demonstrate the effectiveness (enhancement $>10^6$) and reproducibility (better than 10%) of these

nanostructured substrates for SERS using benzenethiol and aminothiophenol molecules as monolayer chemical markers [6].

2. Experimental design

In order to gain a detailed understanding of plasmons on such periodic nanostructures, it is necessary to measure the full dispersion characteristics. Limiting the acquisition to a single frequency or incident angle can lead to misinterpretation of the data such as momentum gaps [7], or miss localised modes which are non-dispersive [8]. Here we present specular reflection spectra recorded across the visible and near infrared spectral region as a function of incident angle, lattice orientation, pit depth and polarisation. White light, ranging from 490nm to 1.7μm, produced by a microchip laser and nonlinear photonic crystal fibre was focused onto the nanostructured samples by a 300mm focal length lens, producing a spot size of 250μm in diameter. Collected light was then focussed on a multimode fibre connected to an Ocean Optics spectrometer with 1nm spectral resolution. The sample was mounted in a previously-developed automated goniometer [5] in which both incident and azimuthal angle can be varied by rotating both sample mount and detector arm. The specular reflection was recorded for incident angles ranging from θ=0° to 70° and lattice orientation ranging between ϕ=0° to 90° for different positions across the sample.
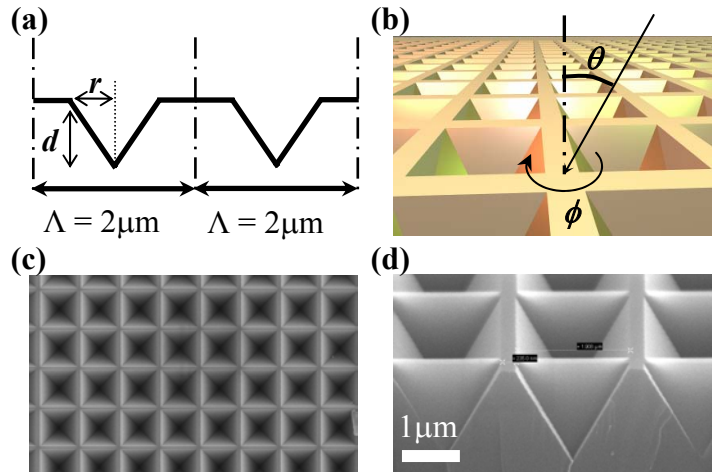

Fig. 1. (a) 2D cross section through the pits, the pitch (Λ) is 2μm. The aperture size (r) and therefore the depth (d) are graded across the sample. (b) Schematic representation of the sample with ϕ orientation of pits and incident angle θ of the laser. (c) and (d) are top and cross section SEM of the sample before metallization.

3. Samples

The nanostructured surfaces consist of a square lattice of inverted square pyramidal pits with a pitch, Λ=2μm and a pit depth ranging from d=0.7μm to 1.0μm. Square and circular apertures in a silicon dioxide mask ranging from 1.0μm to 1.3μm in size were produced using conventional optical lithography on a (100) oriented silicon wafer. Anisotropic etching using KOH was then used to preferentially etch the (111) planes resulting in an array of inverted pyramidal square pits. This fabrication technique is well suited to the production of plasmonic nanostructures for SERS applications because the etched surfaces are extremely reproducible, with the pyramid faces oriented at an inclination α=35.3° to the normal, and atomically smooth [9]. While the pitch remains constant across the sample, the aperture size, r, and therefore pit depth, d=r/tanα, are graded across the surface, to enable identification of the plasmonic features [cross section through pit in Fig. 1(a)]. Figure 1(b) depicts this

nanostructured surface, together with the optical orientation of incident angle, θ, and azimuthal angle, ϕ, relative to the lattice. Figure 1(c,d) show electron micrographs (SEMs) of the silicon surfaces before metallization. A uniform layer of gold (300nm) was RF sputtered onto the samples. The resulting metallic coating was smooth enough to give rise to no hot spots, and therefore no SERS amplification, on the unpatterned planar film regions (as would otherwise be expected from rough gold). The metallization layer was also thick enough such that the pit side walls were electrically connected to the flat top surfaces between the pits.

4. Spectroscopy

By depositing a metallic layer onto these samples we transform the purely-dielectric to a purely-metallic periodically-modulated surface. The metallic layer on the nanostructure now allows propagation of surface plasmon polaritons. In order to clearly identify these modes, we measure reflectivity on the arrays before and after gold coating. The incident light was TM polarised, i.e. electric field oscillates perpendicular to the surface and the collected light was both TM and TE analysed
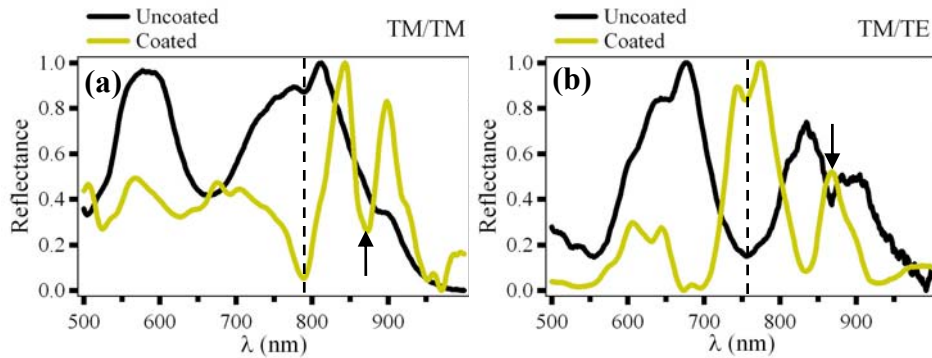

Fig. 2. Reflection spectra at 50° incidence and 3° azimuthal angle for a square array of silicon pits which are uncoated (black) and gold-coated (yellow). (a) TM incident, TM analysed, (b) TM incident, TE analysed. Dotted lines are diffraction features, arrows mark plasmons.

Normalised reflectance spectra (Fig. 2) reveal dramatic differences between gold coated and uncoated samples. Predictable diffraction effects account for some of the observed features (marked with dashed lines). Additional absorption dips (marked with solid arrows) arise from resonant coupling to surface plasmon polaritons. Differences between co-polarized and cross-polarized reflection are observed even for the dielectric grating, (as expected for polarization conversion in the non-normal geometry of the square pits). This polarisation conversion is evident when comparing the spectra: TM/TM dips and peaks are complementary to those in TM/TE configuration. Polarisation conversion is enhanced when plasmon coupling occurs, resulting in strong features in the cross-polarized reflection spectrum [7]. Measured dispersion characteristics for all polarizer/analyser configurations show that TM/TM is very similar to TE/TE and likewise for the cross polarised data (results to be published elsewhere). Hence we concentrate here on TM/TE measurements for our analysis. We have also compared results for circular and square dielectric apertures on the square metallic pits which are also not substantially different (to be published elsewhere).

Comparing reflection spectra from metallic and dielectric surfaces is a clear demonstration of plasmonic effects, but while helpful this data does not provide specific information on the nature of the plasmons. By acquiring reflection spectra as a function of incident angles the dispersion characteristics can be rigorously mapped [5] enabling rapid identification of

diffraction and plasmons modes. Fig. 3 presents an experimental dispersion diagram for TM incident, TE analysed data, for $\phi=45°$ (with the ϕ dependence presented as a movie). Sharp diffraction bands are clearly resolved, appearing with differing strength. Simple grating theory was used to predict the dispersion bands of the structure, Fig. 3(c). These bands were then superimposed upon the experimental dispersion map, Fig. 3(b), to enable a visual comparison to be made. This shows an excellent fit using the measured structural fabrication parameters.
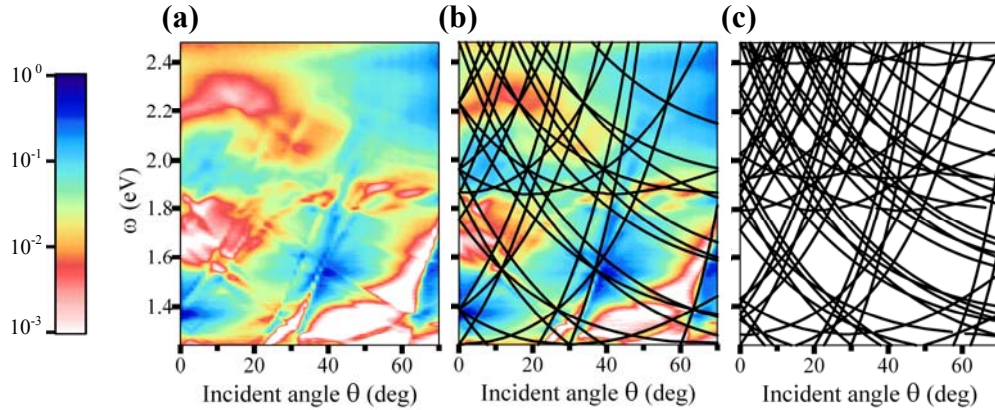
(a)   **(b)**   **(c)**

Fig. 3. (a) Angular dependent experimental reflectivity on Au-coated pit array (colour coded: blue = 100%, white = 0%) for TM/TE at $\phi=0°$, (b) combined plot of (a,c), (c) Grating theory modes up to 5th order. Animated data of (a) as a function of azimuthal angle ϕ is available as a multimedia file (1.5Mb)

The diffraction bands are calculated using an empty lattice approximation, which identifies the (ω,θ) position of all possible bands (which are numerous for 2μm pitch 2D structures), but does not give information on the strength of diffraction. The in-plane $\boldsymbol{k}_\parallel$ of the light which is diffracted from each reciprocal lattice vector, $\boldsymbol{G}[p,q]=p\boldsymbol{a}^*+q\boldsymbol{b}^*$, where $|\boldsymbol{a}^*|=|\boldsymbol{b}^*|=2\pi/\Lambda$, is given by $\boldsymbol{k}_\parallel=\boldsymbol{k}_0\sin\theta\pm\boldsymbol{G}[p,q]$ with $|\boldsymbol{k}_0|=2\pi/\lambda$. The success of this model is evident when we analyse the uncoated dielectric structure, Fig. 4(a), for which the theoretical curves match the experimental diffraction over the full range of incident and azimuthal angles. Comparing this to the coated structure in the identical geometry, Fig. 4(b), we see that while some diffraction lines are now stronger, many modes are strongly energy shifted while new plasmon modes appear.

In order to bring out the weak diffraction features observed for the uncoated pit array, Fig. 4(a), the spectra have been differentiated, enhancing sharp features relative to the background. Although peaks/dips thus show up as zero crossings, this reliably tracks the diffraction modes in the angular dispersion which can show up as Rayleigh edges [9]. Diffraction features appear more clearly on the Au-coated pit array, mainly due to the fact that the gold has a better overall reflection efficiency than bare silicon. With the diffraction lines clearly identified, the plasmonic nature of the unfitted features becomes evident.
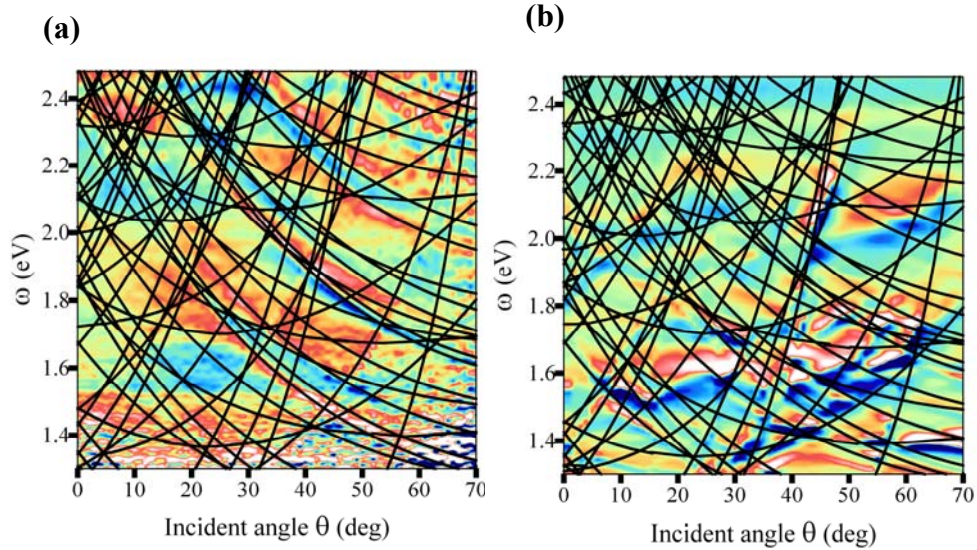
(a)　　　　　　　　　　**(b)**

Fig. 4. Experimental angular dispersion for (a) uncoated and (b) Au-coated pit arrays, together with theoretical diffraction modes. The dynamic range in (a) is 10 times less than in (b). Animated data of (a) as a function of azimuthal angle is available as a multimedia file (2.5Mb)

Closer examination of the dispersion diagrams reveals that some features follow the diffraction lines while others are located in between diffraction bands, this is most obvious in Fig. 3(b). The additional absorptive loss (red/white features) occurs despite the increased reflectivity of gold. Two types of fundamental plasmons can be created on such periodic surfaces: either propagating on the upper planar surfaces, or localised inside the pit [9]. In fact, these modes can couple strongly with each other producing mixed character plasmon modes [5,9]. In order to distinguish localised plasmons, we produce samples in which the pitch and apex angle α are kept constant, but the pit structure is graded linearly both in width and depth. We identify localised plasmons experimentally by measuring their dispersion characteristics as a function of pit depth. In this way, the diffraction bands remain fixed because diffraction processes are governed by the pitch of the structure ($\Lambda\sin\theta_m = m\lambda$), allowing plasmon effects to be easily distinguished.

Further to our experimental investigation, we performed a series of simulations based on a 2D finite-difference time-domain (FDTD) model. While these simulations assume the pits to be infinitely long triangular grooves, they are sufficient to resolve some of the important plasmon physics we observe. Figure 5(a) shows a series of spectra at incident angle θ=0° for pit depths ranging from 750nm to 950nm. A clear shift in absorption dip is observed, with smaller pits giving higher resonant photon energies. Similarly, simulated FDTD spectra, Fig. 5(b), shift towards higher energy with decreasing pit depth. The extracted plasmon energies scale with inverse pit depth, Fig. 5(c), with theory and experiment both identifying two modes, with the same energy spacing, and same dependence on pit depth. However the experimental curves are shifted to higher energy than the simulations by 0.2eV (discussed further below). A confinement-induced energy is expected from plasmons localised in the gold pits. To justify this, we present an additional simple model based on the confinement of propagating surface plasmon polaritons on the sides of a 2D V-groove. Making the assumptions that (a) the sharp convex edge at the top of the pit [T] is an infinite reflecting barrier for surface plasmons, and (b) the sharp concave pit bottom transmits surface plasmons, we can calculate the resonant SPP modes from

$$2a = (m + \tfrac{1}{2})\lambda_{SPP} \tag{1}$$

where λ_{SPP} is the wavelength of the SPPs at energy ω, m is the order of the plasmon mode, and a is the pit wall length. This gives the resonant plasmon energies as

$$\hbar\omega = \frac{\pi\hbar c}{n_{SPP}} \cdot \frac{\cos\alpha}{d} \cdot (m + \tfrac{1}{2}) \tag{2}$$

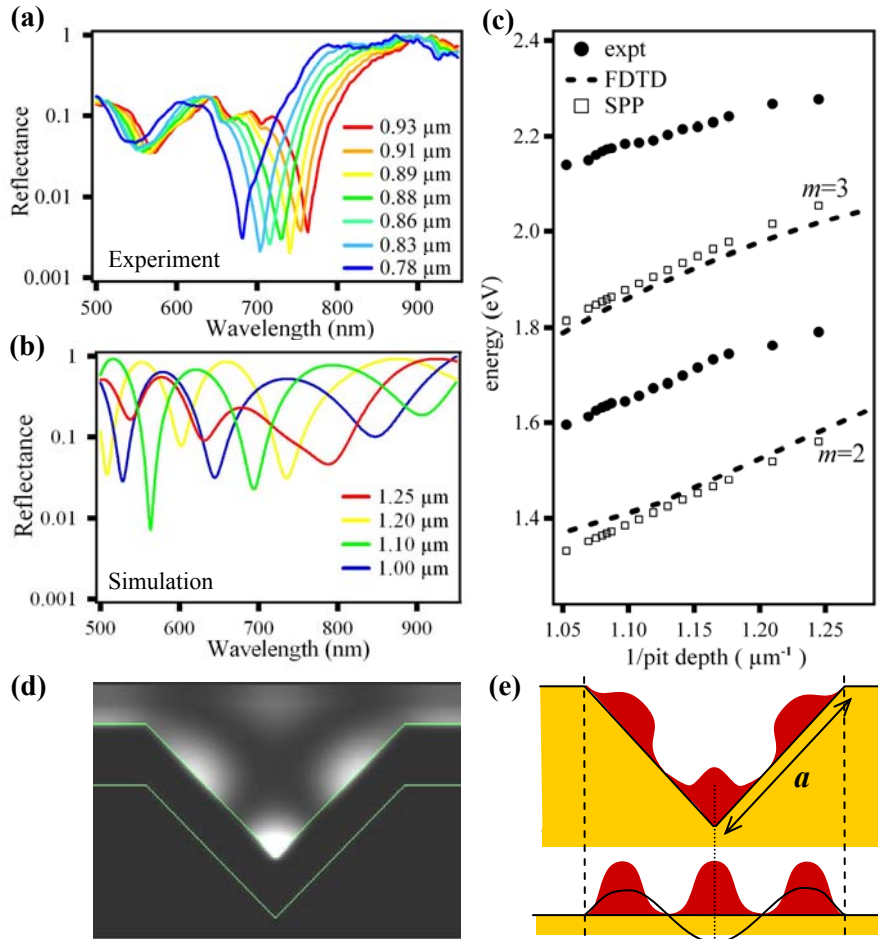where n_{SPP} is the effective refractive index of the SPP modes on flat Au.

Fig. 5. (a) Reflection spectrum vs pit depth at θ=0° for (a) experiment and (b) FDTD 2D simulations at θ=0°. Faint diffraction features common to all spectra are present at 894nm, 708nm, 635nm and 556nm. (c) Extracted plasmon dip energies vs. pit depth. (d) Intensity distribution from FDTD simulation at λ=785nm for d=1250nm. (e) Schematic field (black line) and intensity distribution (filled red) for an m=2 plasmon mode confined in the pit for actual (upper) and un-folded (lower) depiction.

In Fig. 5(c) we plot the first few confined SPP states, which match extremely well the extracted dips from the FDTD model. In addition, this accounts very well for the field

distribution of the localised plasmons. Comparing the $m=2$ mode, Fig. 5(e), which fits 3 half-wavelengths between the upper pit vertices, with the field distribution found at the resonant dip position in the FDTD simulation, Fig. 5(d), gives an intuitive picture of the field distribution. The localised plasmons can thus be approximated by delocalised surface plasmons bouncing up and down the sidewalls of the pit. Specific surface plasmon frequencies are able to form resonant standing wave between the nodes at the top rim of the pits. The difference between the experimental resonance positions and theory can be accounted for from the 3D nature of the square pits - the two orthogonal pit sides to the plasmon oscillation direction squeeze the mode near the pit bottom, producing a phase shift in propagation. In addition, the sharp kink in the surfaces at the apex of the pit concentrates the field distribution just above, thus increasing the total electromagnetic energy. Strong support for this model is the agreement with experiment of the separation of successive nodes in both SPP and FDTD models. While much smaller pits have few modes only at high energy (where the metal absorbs), much larger pits have many modes but their coupling to external photons is weak. Thus in the current size range of the pits, the localised plasmons are conveniently spaced and can be effectively tuned by simple structure design.

This is confirmed when we examine the full angle dependence of the Au-coated pit array at $\phi=45°$, Fig. 6(a,b), which more clearly shows three localised plasmon bands. The sharp features arise from diffraction. These are well fitted by the theory and do not change with pit dimensions. On the other hand, broader plasmon bands are visible (red is increased absorption) which arise from localised plasmons in the pits (arrows, Fig. 6(a)). The non-dispersive property of these modes (their energy is independent of angle) is strong direct evidence for their localisation. The localised modes clearly cross the diffracting modes, and in some cases we see clear evidence for the strong coupling between them. This is more clearly observed by expanding one of the localised-propagating plasmon crossings for samples of graded pit depth but constant pitch, Fig. 6(c). For some orientations, strong coupling is observed in which the new mixed modes are energetically repelled from each other, producing energy ('Rabi') splittings of up to 100meV[5]. The anticrossing evident in Fig. 6, where a flat plasmon band crosses a dispersion line, is similar to the one described by Tan et al [10]. The flat band indicates a localised plasmon band localised in the pits and interacting with the propagating surface plasmon. These flat bands move up in energy as the pit depth decrease. Flat plasmonic band have been previously discussed theoretically in gratings composed of high aspect ratio (20:1) slit structures, in which plasmon waves propagating either side of the groove form a coupled mode and result in a standing wave localised in the groove. The localised mode described here is not dependent on coupling between opposite faces of the pyramidal pits, and the intense field anti-nodes are thus significantly more accessible than deep narrow slits, which are also hard to fabricate reliably. Systematic results at other azimuthal angles confirm the presence of these flat bands. The strength of the observed flat bands is indicative of the very effective coupling process between incident light and localised plasmons [9].
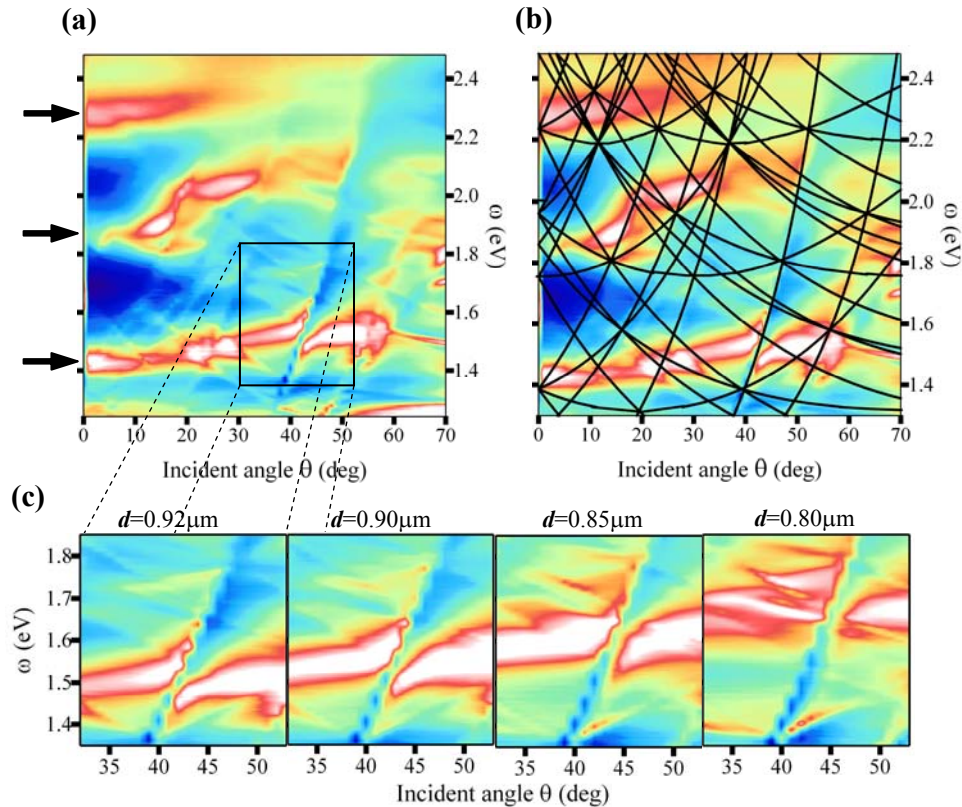
Fig. 6. (a) Angular dispersion of reflectivity on Au-coated pit array for ϕ=45° and d=920nm, with (b) superimposed diffraction curves. (c) Strong coupling observed in angular dispersion of samples with increasing pit depth. Animation of (b) as a function of decreasing pit depth is available as a multimedia file (1Mb)

5. Surface enhanced Raman scattering

Localised plasmon modes are highly suited for use in sensor applications such as SERS. It is well known that plasmons are ideal for transducting incident electromagnetic radiation into molecules, enhancing the Raman scattering process by many orders of magnitude. Incident light excites localised plasmons, which excite molecular dipoles that then lose packets of energy to particular phonon vibrations. These molecular dipoles subsequently re-emit red-shifted plasmons, which are re-emitted back into photons [12]. The detailed SERS dependence of these plasmon substrates is deferred to a separate publication. Instead here we demonstrate the effectiveness and reproducibility of these SERS substrates.

Au-covered pit arrays were immersed in benzenethiol to form a convenient self-assembled monolayer on the gold surface [13]. Raman spectra were then acquired using a commercial (Renishaw) Raman spectrometer for various spatial positions across a 5mm×5mm sample of the pits, using 10s integration times with 3mW of 633nm laser radiation focussed with a ×20 objective, Fig. 7. No signal could be identified on the flat gold-coated section of the sample away from the pits, verifying the importance of the plasmons in the pits for amplifying the vibrational signals from the attached molecules. We have independently verified that the surface morphology of the gold is comparable on the pit faces and on the flat control regions using high-resolution scanning electron microscopy. The measured Raman lines match extremely well to values in the literature and the peak positions are reproducible to within the

spectral accuracy of the system. The Raman signals are extremely reproducible across the entire sample, with less than 10% residual standard deviation in the peak heights from measurement point to measurement point. We also checked the reproducibility sample to sample and found it to be better than 10%.
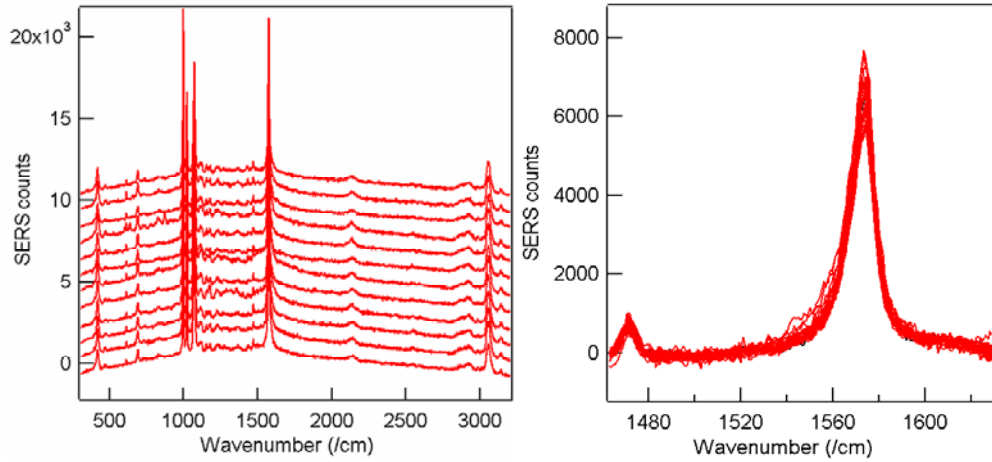

Fig. 7. Raman scattering from a monolayer of benzenethiol on a pit arrays with depth=1μm, for 3mW of 633nm laser, integration time is 10s. (a) Spectra scanned across pit array, shifted vertically for clarity, (b) spectra across pit array, for 1572cm^{-1} line, background subtracted.

The effect of localised plasmon resonances is clearly observed on graded pyramid samples (fig. 8). Here we show the Raman spectrum of monolayer coverage of aminothiophenol, as a function of pyramid depth. It can be clearly seen that as the localised plasmon comes into resonance with the exciting pump laser, the SERS spectrum is further enhanced [5]. However, full understanding of this dependence is complicated by the averaging effect from typical commercial Raman instruments which sum over a wide range of collection angles (and hence the plasmon dispersion shown above). While the Reflection data is taken with an angular collection range of Δθ<0.5°, our standard Raman instrument has an angular collection range of Δθ>60°, folding together many of the resonances seen in the reflection maps. Further measurements are underway in a new angle-resolved SERS geometry to more precisely show the effects of plasmon 'beaming' into different directions [12].
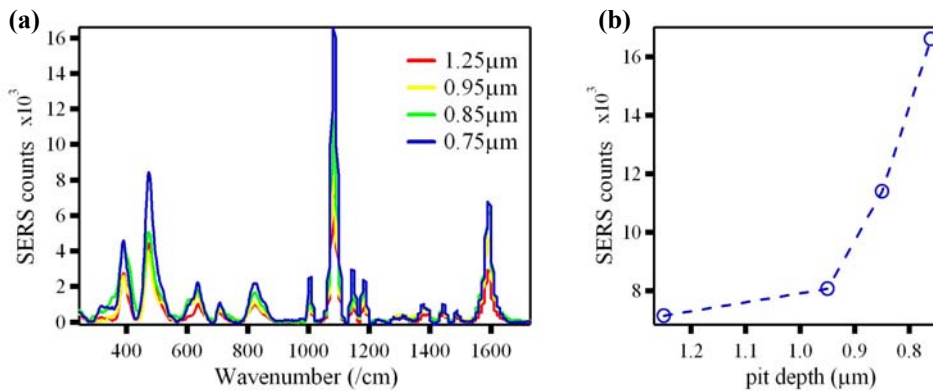

Fig. 8. (a)Raman scattering of a monolayer of aminothiophenol as a function of pit depth, for 785nm excitation wavelength. (b) SERS signal as a function of pit depth for the 1080 cm^{-1} line.

We have also demonstrated the suitability of these SERS amplification substrates for detecting glucose, urea, DNA oligomers and a number of other biochemical targets. Work is currently in progress to quantify the minimum detectable molecular concentration in optimised nano-structures. Although the SERS enhancement of approximately 10^6 in these first nanostructures (measured using standard techniques in a confocal Raman geometry[6,14]) is not the largest seen for SERS [14, 15], much of the problem for practical implementation of SERS has been its irreproducibility [6]. By making plasmons localised in void structures, rather than at sharp nanoparticle tips or between nm-spaced nanoparticles, plasmons can be reliably controlled producing moderate amplification which is quantifiable. In addition, because the plasmon field distributions can also be spatially controlled they can be matched to reach deep inside larger molecules of interest. With this capability, a host of novel additional problems arise, since before exposure to the target molecules the SERS substrates are highly sensitive to the fabrication environment and any background contamination can be seen in the Raman spectra. On the other hand this demonstrates the wide applicability of these substrates to evaluating the signatures of trace chemical contaminants as well as in pharmaceuticals and health biotechnologies.

6. Conclusion

Metallo-dielectric photonic nanostructures have been shown to possess plasmon excitations which can be reliably controlled. By comparing un-coated and gold-coated pyramidal pit arrays, we have resolved the diffraction features from the plasmonic bands. From the comprehensive measurements of the angular dispersion of these structures we distinguish a class of localized plasmons whose energies depend on the pit dimensions. We have also shown (using a simple model) that confined propagating plasmons up and down the pit walls can account for the data, and agree well with a 2D FDTD simulation of the 2D structure. We have demonstrated how the plasmons produce amplification of SERS signals, giving highly reproducible Raman vibrational spectra. This opens up a wide space of applications in which the signature of the detected molecules allows their identification in real time.

Acknowledgments